

Review

Recent progress in solar-driven interfacial water evaporation: Advanced designs and applications

Liangliang Zhu^{a,b}, Minmin Gao^a, Connor Kang Nuo Peh^a, Ghim Wei Ho^{a,c,d,*}^a Department of Electrical and Computer Engineering, National University of Singapore, 4 Engineering Drive 3, 117583, Singapore^b State Key Laboratory of Materials-Oriented Chemical Engineering, College of Chemical Engineering, Nanjing Tech University, 5 Xin Mofan Road, Nanjing 210009, PR China^c Engineering Science Programme, National University of Singapore, 9 Engineering Drive 1, 117575, Singapore^d Institute of Materials Research and Engineering, A*STAR (Agency for Science, Technology and Research), 3 Research Link, 117602, Singapore

ARTICLE INFO

Keywords:

Photothermal conversion
 Interfacial water evaporation
 Solar-driven steam generation
 Desalination
 Water purification
 Energy generation

ABSTRACT

Solar water evaporation plays a central role in low-energy fresh water production which is essential for both human health and economic development. The utilization of photothermal materials with broad solar absorption, in parallel to engineered evaporator designs, offers new approach to achieve efficient light-to-vapor conversion. Thereinto, the stratagem of interfacial water evaporation with the localized heating and restrictive heat losses, has gained wide recognition as an effective avenue towards high-performance sustainable solar steam generation. In this review, we discuss photothermal conversion processes of various solar absorber materials and the conceptual designs of different interfacial photothermal evaporation pertaining to judicious optical, thermal and wettability management, and finally the current progress in scalable saline water desalination, wastewater purification and energy generation applications. This review aims to provide a comprehensive summary of the recent development in interfacial photothermal evaporation and to inspire research efforts/translations from laboratory to practical large-scale solar-driven clean water production. Furthermore, the opportunities of solar water evaporation should be explored beyond silos so as to conjointly address the interlinked water, energy and environmental nexus.

1. Introduction

Fresh water is recognized as a global issue of strategic relevance, which is critical to the humankind's survival, as well as the economic development and societal progress [1]. So far, a large number of people is suffering from fresh water shortage due to population growth, climate changes, and rampant pollution in the last decades [2,3]. Nevertheless, water is one of the most abundant chemical compounds on the Earth, 71% surface of which is covered by water, however mostly oceans and seas are too salty to drink. Consequently, large-scale, efficient technologies of seawater desalination are urgently needed. Traditional desalination technologies include membrane-based designs such as reverse osmosis (RO) [4,5], and thermal-based designs like multi-stage flash (MSF) [6] are economically and geographically unfeasible for off-grid villages or remote regions. This is due to high energy consumption, costly infrastructure and installations as well as inaccessibility. On the contrary, solar vapor generation using sunlight as the only energy source is emerging as a promising and environmentally benign solution,

inspired by the natural evaporation — a vital hydrologic cycle of replenishing the land freshwater supply [7]. However, due to the poor optical absorption of water and acute heat losses, the natural light-to-vapor conversion efficiency is too low to generate practical amount of fresh water supply. Many efforts have been invested in developing advanced solar steam generation systems with highly improved efficiency through the rational designs of photothermal nanomaterials and evaporation systems that utilize the concept of interfacial heating [8–14]. In this way, the broadband solar spectrum is efficiently absorbed and heat loss to the environment is largely suppressed, resulting in the enhancement of solar evaporation efficiency. Moreover, the solar steam generation can be used for electricity generation, medical sterilization or sanitization and wastewater purification [15–19]. This suggests that the solar-driven evaporation technology may provide potential opportunities for fresh water and green energy production.

* Corresponding author at: Department of Electrical and Computer Engineering, National University of Singapore, 4 Engineering Drive 3, 117583, Singapore.
 E-mail address: elehgw@nus.edu.sg (G.W. Ho).

<https://doi.org/10.1016/j.nanoen.2018.12.046>

Received 7 November 2018; Received in revised form 11 December 2018; Accepted 11 December 2018

Available online 16 December 2018

2211-2855/ © 2018 Elsevier Ltd. All rights reserved.

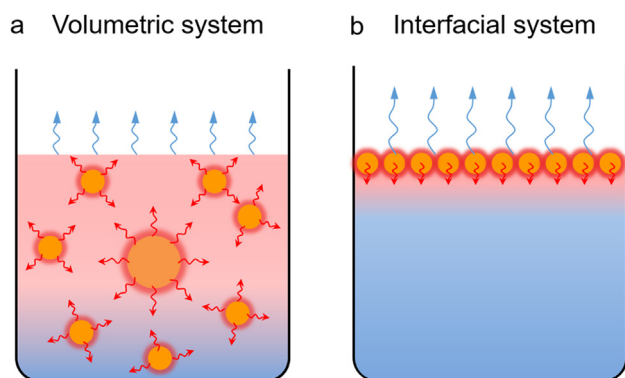


Fig. 1. Schematic drawing of various photothermal evaporation systems; (a) the volumetric system and (b) the interfacial system.

1.1. Interfacial solar steam generation (ISSG)

Generally, in a solar-driven evaporation system, solar energy is received and absorbed by a solar absorber (photothermal materials), and then converted into thermal energy, which is used to heat up liquid water to generate vapor [14,20]. In the context of the location of the photothermal material is being placed in the working fluid, solar steam generation systems can be classified into two categories (Fig. 1) [7]. The first category is a suspending system where photothermal materials are dispersed in the bulk water, known as a volumetric system (Fig. 1a). This system typically relies on costly and cumbersome optical concentration systems to enable bulk heating of a liquid. The hot bulk water is prone to various heat losses, and the unnecessary heating of the portion of the liquid that does not participate in steam generation, resulting in relatively low efficiencies [14,21]. The second one is an interfacial solar steam generation (ISSG) system with the photothermal materials separated from the bulk working fluid (Fig. 1b), which will be the focus of this review.

In the ISSG system, both the solar energy harvesting and steam generation are localized at the water-air interface by using solar absorbers. The solar absorbers are thermally insulated by either directly floating at the water surface or linked to the bulk water through a confined water path [22,23]. The converted thermal energy is restricted at the interface and only heats up the surface water. In this way, the heat losses are suppressed in the interfacial system in two ways: (1) the temperature of the absorber in this system is lower, thus reducing radiation and convection heat losses on the absorber surface; (2) the temperature of the bulk liquid is close to the ambient temperature, minimizing heat loss from bulk water to the environment and eliminating the use of converted thermal energy to heat up water that does not participate in steam generation [14]. With this scheme, solar-to-steam conversion efficiencies of more than 90% have been reported in the recent studies [13,19,24–28].

Herein, we review the recent progresses made in the development of the solar-driven interfacial evaporation and the advanced concepts of pertinent photothermal converting materials and system designs. The characteristics of this review include: (1) The current achievements of efficient systems based on tactical designs of materials and structures are reviewed in detail for the first time; (2) the applications in seawater desalination, wastewater purification and energy generation are also summarized ground on the practical scalable materials and systems; (3) the challenges and perspectives of high-performance ISSG are also discussed. The goal of this review is to provide recent accomplishments and guidelines towards the designs of efficient solar absorber nanomaterials and system engineering for better deployment of solar-driven interfacial evaporation.

2. Photothermal conversion mechanisms and steam generation efficiency calculation

2.1. Photothermal conversion mechanisms

Nanostructured photothermal materials for harvesting solar illumination is an emerging approach for water vaporization. The photothermal effect induced by the nanostructured material can downsize the defined region of heat modulation to nanoscale. Moreover, the nanomaterials possess unique electronic and optical properties, leading to localized surface plasmonic resonance, quantum confinement effects and other intriguing phenomena. Based on the different interaction between electromagnetic radiation and matter, three photothermal conversion mechanisms i.e. plasmonic localized heating of metals, non-radiative relaxation of semiconductors and thermal vibration of molecules are presented [18].

2.1.1. Plasmonic localized heating of metal

In some metallic nanomaterials, the localized surface plasmon resonance (LSPR) effect is exhibited, which is a resonant photon-induced coherent oscillation of charges occurring when the photon frequency matches the natural metal surface electrons frequency [29]. Three sequential phenomena including near-field enhancement, hot electron generation and photothermal conversion are induced by the LSPR effect [30–32]. The plasmon-assisted photothermal effect occurs when metal nanoparticles are illuminated at their resonance wavelengths, which causes oscillation of the electron gas. The electrons are excited from the occupied states to unoccupied states, forming hot electrons [33]. Rather than through radiative emission, the decay of these hot electrons through electron–electron scattering redistributes the hot electron energy which can rapidly increase the localized surface temperature of the metal particles [18,34]. This localized temperature transfers into the particle lattice through electron–phonon interactions at a time scale of 2–5 ps, followed by phonon–phonon interactions with the surrounding medium at a time scale of 100–380 ps [35]. The LSPR effect is strongly correlated to the shape, size, dielectric coatings or medium around a particle and the assembly state. Generally, the hollow structures or shape asymmetry could broaden the spectral LSPR band, while variations in particle size or the surrounding dielectric induce LSPR band shift and possibly broadening of the absorption band [7]. So far, gold and silver are the most common plasmonic metal adopted for photothermal vaporization [30,36,37]. Gold displays excellent visible-near infrared (NIR) plasmonic resonances and chemical stability, while silver exhibits high plasmonic resonance response and low plasmonic losses in the optical frequency regime. Besides, other metals have been developed for a wide range of plasmonic applications, such as aluminum, copper, cobalt, nickel and platinum [24,38–40].

2.1.2. Non-radiative relaxation of semiconductors

It is well known that electron–hole pairs are produced when a semiconducting material excited by an energy similar to the bandgap under the light illumination. When the excited electrons eventually return to the low-level states, energy is released by transferring to impurities/defects or surface dangling bonds of the material through either radiative relaxation in the form of photons, or non-radiative relaxation in the form of phonons [41]. When the energy is released via phonons, it can induce a local heating of the lattice which establishes a temperature distribution according to the optical absorption and bulk/surface recombination characteristics. As a result, the photothermal effect is displayed in the material by the optically excited diffusing and recombining carriers [18]. Metal oxides and chalcogenides have shown promising prospects due to fine tunability in their absorption spectrum and large extinction coefficients in the NIR region. Up to now, Cu_7S_4 [42], $\text{Cu}_{12}\text{Sb}_4\text{S}_{13}$ [43], HCuPO [44], Cu_2SnSe_3 (or $\text{Cu}_2\text{ZnSnSe}_4$) [45], titanium-based semiconductors (black TiO_2 [46], black TiO_x [47], and narrow-bandgap Ti_2O_3 [27]), magnetic particles (Fe_3O_4 , MnFe_2O_4 ,

ZnFe₂O₄, and CoFe₂O₄) [48–50], BiInSe₃ [51], SnSe [52], Al–Ti–O [53], NiO [54], and MoO_{3-x} [55] et al. have been reported and validated as effective photothermal evaporation materials.

2.1.3. Thermal vibration of molecules

In many organic materials, heat is generated through lattice vibration by absorbing optical energy [18]. However, energy gaps between σ and σ^* of most single carbon bonds including C–C, C–H, and C–O are too large, corresponding to wavelengths below 350 nm, to realize the σ to σ^* transition under solar irradiation. While π bonds are usually weaker than σ bonds owing to less strongly bonded electrons, as such it is possible to excite π to π^* with a lower energy input. The conjugated π bonds can cause a red-shift in the absorption spectrum. Whilst increasing the number of π bonds can decrease the energy gap between the highest occupied molecular orbital (HOMO) and the lowest unoccupied molecular orbital (LUMO). In graphene-like allotropes, a large number of conjugated π bonds enable the excitation of electrons by almost every wavelength of the solar spectrum, bringing about various π – π^* transitions and exhibiting black color appearance. When the input light energy matches an electronic transition within the molecule, the electron absorbs the light and is promoted from the HOMO to LUMO. The excited electrons relax via electron–phonon coupling and the energy is hence transferred from the excited electrons to vibrational modes throughout the atomic lattices, resulting in a macroscopic temperature rise of the material [56]. Miscellaneous carbon-based photothermal materials such as carbon nanotubes (CNTs) [57–59], graphene [26,60], graphene oxide (GO) [61], reduced graphene oxide (rGO) [62,63], carbon black [64–67], carbon fabric [68], carbon beads [10], foams [69,70], sponges [19] and carbonized natural products [71–73] were reported to be superior light absorbers for interfacial water evaporation.

2.2. Steam generation efficiency calculation [19,21,60]

The overall steam generation efficiency (η) can be calculated using the Eq. (1):

$$\eta = (\dot{m}h_{LV})/q_i \quad (1)$$

where \dot{m} is the solar-driven evaporation rate of water under solar illumination ($\dot{m} = m_{\text{light}} - m_{\text{dark}}$), q_i is the incident power density of solar illumination in process of steam generation experiment, and h_{LV} made up of the sensible heat and the enthalpy of vaporization is calculated using the Eq. (2):

$$h_{LV} = C\Delta T + \Delta h \quad (2)$$

where C is the specific heat capacity of water and a constant of $4.18 \text{ J g}^{-1} \text{ K}^{-1}$, ΔT is the temperature increase of water, and Δh is the enthalpy of vaporization on the relative temperature.

3. Development of advanced interfacial system design concepts

The heat transfer process of ISSG involves three energy flows: solar energy input, vapor output, and heat exchange with the environment [13]. Thereby, the key factors associated to efficient ISSG system are effective solar energy absorption and conversion, adept water transport from bulk to the surface, and minimal heat loss at both sides of the steam generation interface [14]. To achieve a high efficiency solar vaporization, various advanced photothermal materials and rational system designs from enhanced energy input to optimized heat management have been developed. In this section, we will discuss several efficient system design concepts to enhance solar absorption, heat management and wicking efficiency for highly efficient solar water vaporization (Fig. 2). The photothermal materials and vaporization efficiency based on the advanced system design concepts reported in recent literatures for interfacial water evaporation have been summarized in Table 1.

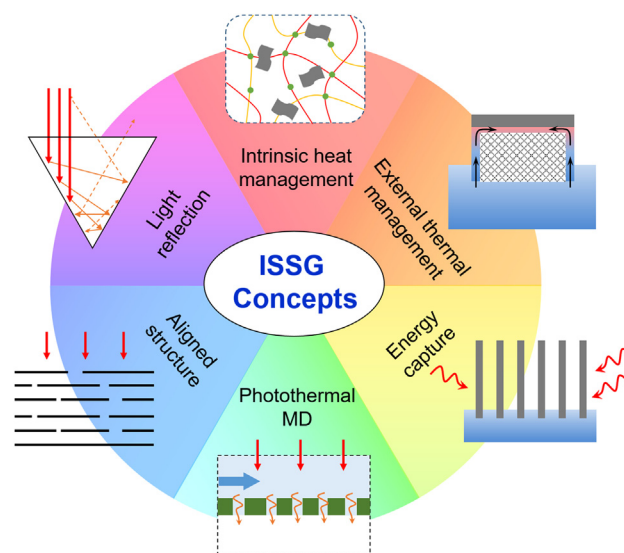


Fig. 2. Schematic diagrams of the advanced system design concepts.

3.1. Optical enhancement

Solar absorptance is a critical parameter of light-to-heat conversion, which determines the amount of initial energy input. Photothermal solar evaporation requires the light absorber materials to possess efficient and broadband optical absorption across the full solar spectrum range (from 250 to 2500 nm) with minimal transmittance and reflectance. Besides the intrinsic property of solar absorber materials, rational structural design at the macroscopic and microscopic level are essential to achieve high solar absorptance. Many efforts have been devoted to develop superior solar absorber materials and structures with low overall reflectance through delicate tuning of solar absorber composition, designing of multilayer coating, and engineering of surface/integral structures [63,74,75]. In general, flat planar photothermal material only permits a single reflection due to its smooth surface, leading to a low solar absorptance. For instance, a densely stacked graphene membrane showed a weak light absorption because of its planar reflection [63]. Hence, rough surface/texture and three-dimensional (3D) architected solar absorbers have been designed and employed to enhance the solar absorptance by reclaiming/recycling of multiple light reflections [63,75,76]. Accordingly, Wang et al. constructed a carbon-based photothermal layer with a rough surface using two-dimensional (2D) reduced rGO and one-dimensional (1D) multi-walled carbon nanotubes (MWCNTs) [63]. By tuning the content of the added MWCNTs, the surface roughness and loose structure of the rGO–MWCNT photothermal layer can be controlled and optimized, which exhibited enhanced solar irradiation absorption by reducing light reflection, as shown in Fig. 3a. As a result, the diffuse reflection of the rGO–MWCNT composite layer decreased to 4.7% with 88 wt% MWCNT, compared to 13.3% diffuse reflection of the pure rGO layer. Such low light reflection photothermal layer was attributed to the augmented light absorption of the CNTs and the additional surface texturing. The corresponding surface temperature is over 10°C higher than that of pure rGO layer. Likewise, other rough surface structures, including porous films [77,78], foam [28,79–81] and sponge [19] are reported for efficient light absorption and photothermal water evaporation. Apart from the surface roughness and loose structure, unique 3D integral structures have also been reported, such as the cup and conical structures [75,76]. The multiple reflections of the incident light occur within the cavity of the cup or cone, contribute to the enhancement in light absorbance. A 3D cylindrical cup-shaped structures composed of mixed metal oxide reported by Wang's group have exhibited superior energy efficiency close to 100% under 1 sun illumination [75]. The cup-

Table 1
Interfacial water evaporation efficiency based on different design concepts from the selected typical publications.

Materials	Efficiency (%)	Solar intensity (kW m^{-2})	System design concepts ^a	Reference
Black cellulose fabric	57 ± 2.5	1	Ext.	[2]
Cotton cores/carbon black-coated cellulose paper	240/150/110/100	0.25/0.5/1/1.2	Env.	[13]
Au nanoflowers/silica gel	85	1	Int.	[17]
Carbon sponge	90	1	Opt./Int.	[19]
Al NPs/AAM	88.4/91	4/6	Opt./Ali.	[24]
PVA/PPy hierarchical gels	94	1	Int.	[25]
Vertically aligned graphene sheets membrane	86.5/94.2	1/4	Ali./Ext.	[26]
Hierarchical graphene foam	91.4	1–5	Opt.	[28]
Au/Al ₂ O ₃ template	90	4	Opt./Ali.	[36]
Plasmonic wood	85	10	Opt./Ali.	[37]
TiAlON based nanocomposite/NiO disk	73/90	1/4	Ext.	[54]
CNT-modified flexible wood	81	10	Ali.	[58]
3D-printed GO-based evaporator	85.6	1	Ext.	[59]
rGO–MWCNT based membrane	80	1	Opt.	[63]
Carbon black coated paper	88	1	Ext.	[66]
Carbon black in PVA	53.8	0.7	PMD/Opt.	[67]
Carbonized mushrooms	78	1	Opt./Ext.	[71]
Flame-treated wood	72/81	1/3	Ali.	[72]
Carbonized wood	86.7	10	Opt./Ali.	[73]
Cup-shaped structure of mixed metal oxide	140	1	Opt./Env.	[75]
Cone-shaped of PPy	93.8	1	Opt.	[76]
3D graphene networks/wood	91.8	1	Opt./Ali.	[77]
Ag/diatomite/airlaid paper	92.2	1	Opt./Ext.	[78]
3D honeycomb graphene foam	87	1	Opt.	[79]
rGO/polyurethane foam	81	10	Opt.	[80]
Hierarchical graphdiyne-based architecture	91	1	Opt.	[81]
Black carbonized wood	91.3	1	Opt./Ali./Ext.	[82]
Graphite/wood	80/89	1/10	Ali.	[85]
surface-carbonized longitudinal wood	89	10	Ali.	[86]
Vertically aligned graphene pillar array	95	1	Ali.	[87]
Au NPs/filter paper	89	10	Ext.	[88]
Ink-stained paper	85.8/85.5	1/3	Ext.	[89]
Carbon black/GO	87.5	1	Ext.	[90]
rGO/filter paper	89.2	1	Ext.	[91]
Defect-abundant graphene sheets	91	1	Ext.	[92]
GO film/cotton rod	85	1	Ext.	[93]
GO film/cellulose paper	80	1	Ext.	[94]
Porous rGO layer	83	1	Ext.	[95]
TiO ₂ -PDA/PPy/cotton	98	1	Ext.	[96]
rGO–silk-fabric	102	1	Ext.	[97]
Carbon powder coated paper	122 (2.02 kg m ⁻² /h)	1	Ext./Env.	[98]
rGO in PVA network	95	1	Int.	[99]
Commercial absorber (Bluetec)/PVA/Electrospun PVDF-HFP nanofibers membrane	72	1	PMD	[102]
PVDF/Ag NPs	–	–	PMD	[103]
Carbon black NPs coated PVDF membrane	74.6	1.3	PMD	[104]
Dye modified PTFE membranes	60	1	PMD	[105]

^a Opt.: Optical enhancement; Ali.: Aligned structures; Ext.: External confined water path and insulation; Int.: Intrinsic water path and insulation; Env.: Environmental energy enhancement; PMD: Photothermal membrane distillation.

shaped 3D structure favorably recovers most of the diffuse reflected light from the bottom to hit the cup wall and then be largely absorbed by the wall (Fig. 3b), which greatly reduced the energy loss caused by diffuse reflection. Similarly, Jiang's group demonstrated a 3D photothermal cone with a polypyrrole (PPy) coating layer for high-efficiency solar-driven evaporation [76]. The 3D cone exhibited high absorbance around 99.2% in the entire solar spectrum due to the multiple reflections. Similar to the cup-shaped structure, a photothermal cone with an appropriate angle of apex can lead to multiple light reflection-absorption, finally resulting in almost total absorption of incident light.

Besides that, columnar microstructures have demonstrated prominent light absorption for the whole solar spectrum. The columnar microchannels provide strong scattering and internal reflection, which further boost the absorption efficiency. Natural wood has vertically aligned microchannels and interconnected pore networks which enable efficient water transport and waveguide effect [37,73,82]. The diameter of the aligned microchannels in natural wood is much larger than light wavelengths (from 5 to 50 μm), allowing different light wavelengths to pass through, thus facilitating broadband light absorption. Hu's group exploited a plasmonic wood (basswood) by loading fine

metal nanoparticles into the matrix of natural wood [37]. After the incorporation of various noble metals (Pd, Au and Ag nanoparticles), the plasmonic wood achieved a high solar absorption (99%) across a wide wavelength range (200–2500 nm). The plasmonic effect of metal nanoparticles and the waveguide effect of microchannels in the wood matrix play significant role in promoting light harvesting (Fig. 3c). Moreover, the absorption was angle-independent owing to the repeated light reflection/scattering and absorption along the unique columnar microstructures of the wood. Similarly, the nanoporous anodic aluminum oxide (AAO) template functions as an efficient light trapping medium, which strongly scatters the light through the internal reflections, extending the path length of incident light within the nanoporous structure [24,36,83,84]. Zhu's group designed closely packed Au plasmonic particles with random sizes and distributions into the AAO aligned nanochannels, enabling a high density of hybridized LSPR, which gave rise to broadband absorption (Fig. 3d) [36]. Together with the strong scattering and internal reflection within the nanoporous template, an impressive average light absorbance of 99% across the visible to mid-infrared regimes (400–10 μm) was achieved.

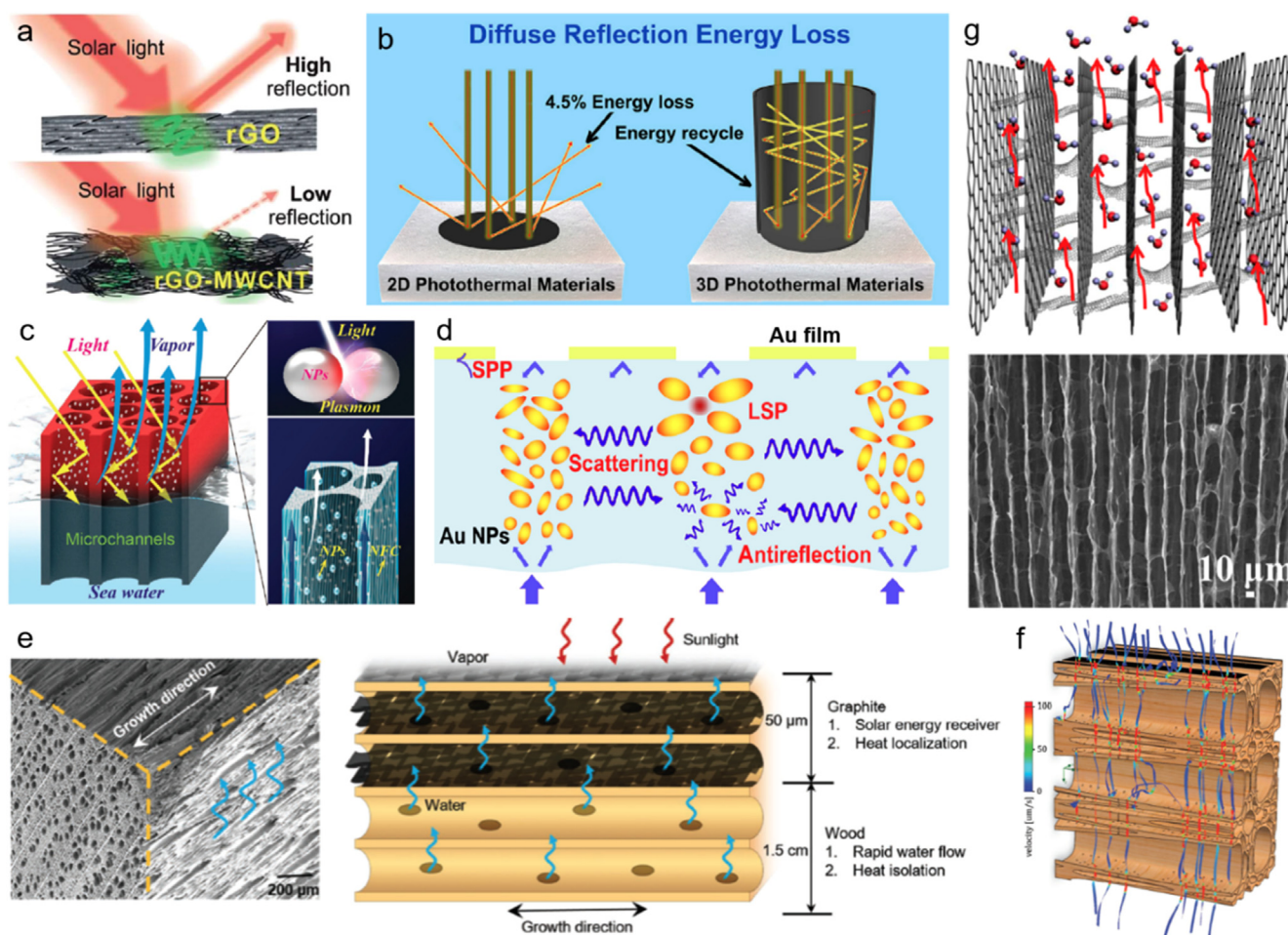


Fig. 3. (a) Schematic illustration of the photothermal layer to reduce the light reflection [63]. Reprinted with permission from Ref. [62]. (b) Schemes of diffuse reflection for photothermal materials with 2D disk and 3D cup structures, demonstrating that the cup wall can efficiently recycle the diffuse light reflection [75]. Reprinted with permission from Ref. [74]. (c) Design of plasmonic wood with both the plasmonic effect of metal nanoparticles and the waveguide effect of microchannels in the wood matrix [37]. Reprinted with permission from Ref. [36]. (d) Schematic of a plasmonic absorber with Au nanoparticles of random sizes and distributions for the LSPR effect and nanoporous AAO templates for efficient reflection reduction and scattering [36]. Reprinted from ref. 35. (CC BY-NC 4.0). (e) SEM image of mesoporous wood with the wood lumens aligned along the wood growth direction and schematic showing the solar steam generation mechanism of the graphite-coated wood [85]. Reprinted with permission from Ref. [83]. (f) Water transport trajectories across lumens shown in a 3D mesoporous basswood structure colored by velocity magnitude. (g) Mechanism illustration and SEM image of VA-GSM for the solar steam generation [26]. Reprinted with permission from Ref. [25].

3.2. Aligned structures: Vertical and horizontal alignment

As mentioned above, the vertically aligned microchannel structures in natural wood and AAO template are designed for multiple internal light reflections to enhance the light absorption. Furthermore, the vertically aligned microchannels play an important role in excellent thermal insulation and water transportation from the bulk water body to the evaporation surface by the capillary action [72,73,77]. The 3D mesoporous plasmonic wood has a low thermal conductivity of $\sim 0.46 \text{ W m}^{-2} \text{ K}^{-1}$ along the microchannel direction, which could help to localize the heat on the evaporation surface [37]. As a result, the 3D aligned porous architecture achieved a high solar conversion efficiency of 85% under 10 sun illumination. Moreover, the large diameter of the aligned microchannels in plasmonic wood allow rapid water transport. The cumulative salts which were accommodated in the aligned microchannels could also gradually dissolve back into the saline water and diffuse into the bulk water when the solar lamp is turned off. More interestingly, the anisotropism of mesoporous wood has been investigated by Hu's group [85]. They found that the thermal conductivities of wood with horizontal microchannels was lower than vertical microchannels [37,58,86]. The anisotropic thermal conduction redirected the absorbed heat along the in-plane direction while

impeding the conductive heat loss to the water. Meanwhile, the efficient fluidic transport in the crossplane direction of wood microchannels was facilitated by the even nanoscale pits and spirals which exist horizontally along the large wood lumens. (Fig. 3e-f) A high steam generation efficiency of 80% under 1 sun and 89% under 10 sun were achieved using the graphite coated wood horizontal aligned channels.

Other than those aligned structures created by nature, artificially aligned structures for enhanced solar evaporation are also proposed. Qu's group reported a long-range vertically aligned graphene sheets membrane (VA-GSM) as the highly efficient solar thermal converter for generation of clean water, as shown in Fig. 3g [26]. Compared to both layer-by-layer assembled rGO film and structure-disordered rGO foam, VA-GSM provides open channels that facilitate water transport, high light absorption capacity for excellent photothermal transduction and vapor release. Water evaporation rates of 1.62 and $6.25 \text{ kg m}^{-2} \text{ h}^{-1}$ under 1 and 4 sun, equivalent to outstanding efficiencies of 86.5% and 94.2%, were obtained, respectively. In the same group, a vertically ordered pillar array of the graphene-assembled framework (HOPGF) was also fabricated by the laser processing [87]. The HOPGF possesses ample free space and evaporation area, hence promoting the full directional release of vapor and faster water evaporation. Moreover, the air filling between the pillars served as thermal barriers, resulting in

low thermal conductivity ($18\text{--}35\text{ mW}^{-1}\text{ K}^{-1}$) of HOPGF, which effectively reduced heat loss toward bulk water and the ambient environment. Therefore, a high water evaporation rate of $2.10\text{ kg m}^{-2}\text{ h}^{-1}$ was obtained under only 1 sun.

3.3. External confined water path and insulation

In the ISSG, heat losses between the heated up interfacial medium and bulk water are inevitable due to the contact between the solar absorber and water body. To further suppress heat conduction losses, various structures that separate the solar absorber from water bodies have been designed to improve the energy conversion efficiency. Confined water paths are constructed to link up the solar absorber to the water body for constant water supply and bulk water insulation [7,18]. In nature, plants have the intrinsic ability to transport water and nutrients from the root to the trunk and leaves through the vertically aligned channels, otherwise known as the plant transpiration [54,88]. Inspired by the natural process, the mimetic transpiration system (MTS) was developed by Miao's group for direct efficient solar steam generators, in which spatial isolation was introduced between the insulator and the water. The water transportation took place in the 1D channel via the capillary force, resembling the tree roots. Expanded polystyrene (EPS) foam was employed as the thermal insulator, as shown in Fig. 4a–b [82,88–90]. High-performance and non-toxic ink-stained paper and black carbonized wood photothermal converters were successfully prepared [82,89]. A proof-of-concept MTS generator with ink-stained paper and carbonized wood achieved high conversion efficiencies of 85.8% and 91.3% under 1 Sun respectively, originating from the excellent thermal management of the systems. Similar structures using GO and rGO films equipped with one or multiple wicking 1D fabrics/pipelines coupled to foam thermal insulators were also reported to be efficient solar thermal converters [90–92]. Likewise, other efficient MTS generators with umbrella-shaped structures and air thermal barriers have also been fabricated to minimize heat loss and angular dependence of light absorption [71,93]. 2D water paths can also realize efficient water supply in an interfacial evaporation system by wrapping a thermal insulator with a hydrophilic material to provide a 2D

capillary water pathway to the top of the solar absorber material. Gan's group reported a polystyrene foam (thermal insulator) that was wrapped with carbon black coated paper (2D water path and solar absorber) with the edges of the paper in contact with bulk water [66]. In this way, the isolated solar evaporation system displayed an effective 2D water supply and suppressed heat losses, which enabled an efficient solar desalination ($> 88\%$ under 1 sun). Likewise, hydrophilic porous paper [78,94], carbon-based absorber film [66,95], fabric [2,96,97] and 3D-printed carbon-based walls [59] were also used for efficient interfacial solar evaporation.

3.4. Intrinsic water path and insulation

Besides the strategic external thermal and water supply management to improve the efficiency of solar evaporation, controlling/regulating inherent structures and properties of photothermal materials manifest an intriguing and promising route. The intrinsic hierarchical pores, from molecular mesh- to macro-size, in the photothermal materials (e.g. polymer and silica hydrogel, carbon foam etc.) [17,19,25] play critical roles in tactical management of internal energy transfer, heat flow, and water supply without the assistance of external thermal insulation. In recent works, Yu's group reported a highly efficient solar evaporation based on hierarchically nanostructured gels (HNG) composed of a hydrophilic polymer network (polyvinyl alcohol, PVA) and solar absorber (PPy) with internal gaps, micron channels and molecular meshes existed in HNG's internal structure. (Fig. 4c) [25]. Due to the penetration of solar absorbers in the polymeric gel PVA network, the converted solar energy could be directly delivered to the small amount of water in the molecular meshes under the light irradiation (see 1 in Fig. 4d). PVA chains eliminated the convective heat loss of water, which was the main energy loss avenue in solar vapor generators. Moreover, the rapid water diffusion and capillary pumping by micron channels (see 2 in Fig. 4d) and internal gaps (see 3 in Fig. 4d) led to rapid replenishment of the molecular meshes through swelling of the polymeric network to sustain high rate vapor generation. Importantly, vaporization enthalpy of water confined in the HNG molecular mesh was smaller than that of bulk water. Therefore, a high water evaporation rate of

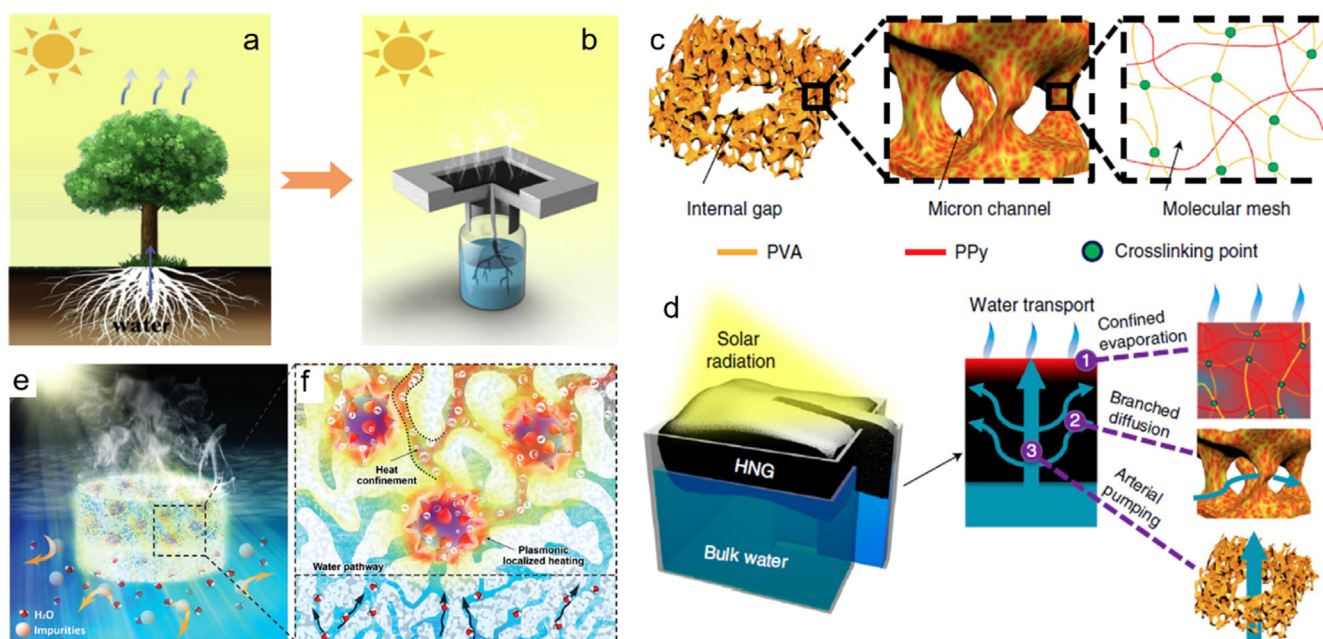


Fig. 4. Schematic illustration of (a) transpiration of trees and (b) MTS under solar illumination for a solar steam generation [82]. Reprinted with permission from Ref. [81]. (c) The HNG consists of hierarchical porous structures, including internal gaps, micron channels and molecular meshes, wherein the solar absorber (PPy) penetrates the polymeric PVA network of the gel. (d) Schematic of a typical solar vapor generation system and the water confinement strategy [25]. Reprinted with permission from Ref. [24]. (e–f) Schematic drawing of the designed solar absorber gel for solar vaporization [17]. Reprinted with permission from Ref. [17].

$3.2 \text{ kg m}^{-2} \text{ h}^{-1}$ was achieved under 1 sun solar radiation, which is much higher than the conventional theoretical upper limit ($\sim 1.65 \text{ kg m}^{-2} \text{ h}^{-1}$ under 1 sun) [98]. Similar work based on PVA framework and rGO revealed a high water evaporation rate of $2.5 \text{ kg m}^{-2} \text{ h}^{-1}$ under 1 sun illumination. Additionally, these molecular meshes enable the evaporator to circumvent water evaporation induced crystallization fouling, hence accomplishing a long-term solar desalination [99].

Silica gel with low thermal conductivity and poor light harvesting is also employed as a good thermal insulator. Ho's group presented an all-embracing integral design of a solar absorber gel, in which solar absorber Au nanoflowers at ppm level were incorporated into low thermal conductivity silica-gel [17]. (Fig. 4e) The multi-porous structures in composite gel provides concurrent macroscopic insulation to prevent heat loss to bulk water, nanoscopic heat confinement at the vicinity of Au nanoflowers, and mesopores for water capillarity and steam permeability. (Fig. 4f) With this design, the evaporation efficiency is $\sim 85\%$ under 1 sun condition. Notably, the 3D open network allows the passage of fluid while blocking off certain dissolved and particulate matters, offering an important antifouling capability. Moreover, a novel elastic macroporous cellular carbon sponge which possesses an inbuilt structural hierarchy with seamlessly interconnected mesoporous fibers was also reported by Ho's group [19]. The components and inbuilt structural features are beneficial to broaden the band of light absorption, soak up and store water. By the sponge capillary action, self-confined water was wicked and transported to perpetual hotspots so as to perform in situ evaporation. Under this system, solitary heat localization without any contact with the bulk water supply is viable so that the thermal isolation effect was strictly enforced. A high efficiency of 90% was obtained, which is higher than conventional suspending configurations.

3.5. Environmental energy enhancement

The ultimate goal for all energy harvesting and conversion applications is to achieve 100% efficiency, corresponding to the evaporation rate of $\sim 1.65 \text{ kg m}^{-2} \text{ h}^{-1}$ under 1 sun [98]. Due to the energy loss from the absorber to the environment via heat exchange, the evaporation rate is lower than that assuming 100% solar-to-vapor energy transfer efficiency. However, it has been illustrated that interfacial solar evaporators with careful structural designs are capable of theoretical breakthrough. These structural designs ensure the temperature of the solar absorber is lower than that of the environment so that extra energy can be gained from the environment, giving rise to the enhanced evaporation rate beyond the theoretical limit (Fig. 5a) [13,75,98]. For this purpose, a cylindrical vapor generator composed of cotton cores wrapped with carbon black-coated cellulose paper was fabricated by Zhu's group, as shown in Fig. 5a-b [13]. The top surface of light absorber absorbed most of incident solar energy, leading to a higher temperature compared with the environment. While the side surfaces of the absorbers didn't absorb much solar energy, along with the evaporative cooling, resulting in decreasing temperature of the side surfaces to lower than that of the environment. Thereby, the side surfaces can harvest energy from the warmer environment through convective and radiative heat transfer processes. By using this vapor generator design, the enhancement factors of 2.4, 1.5, 1.1, and 1.0 were achieved for the light intensities of 25, 50, 100, and 120 mW cm^{-2} , respectively compared with 100% solar-to-vapor efficiency. Likewise, Gan's group reported a cold vapor generation technique with limit-breaking vaporization rates using a carbon-coated paper (CP)-foam system [98]. Under low intensity solar illumination, the total vapor generation rate was higher than the upper limit that can be produced by the input solar energy because extra energy is taken from the warmer environment. Importantly, this breakthrough technique was also realized under the practical 1 sun illumination. A set of triangle structures with different apex angles (θ) were demonstrated to reveal the best-measured rate of

$\sim 2.20 \text{ kg m}^{-2} \text{ h}^{-1}$ for the sample with $\theta = 22.4^\circ$ under 1 sun illumination (Fig. 5c-d), which extracted 20.7% energy from the environment for vapor generation. Based on the same principle, the 3D cylindrical cup-shaped structure led to a high solar evaporation efficiency [75]. By increasing the height of the cup wall, the additional heat was gained from the ambient air under 1 sun, resulting in an extremely high steam generation rate of $2.04 \text{ kg m}^{-2} \text{ h}^{-1}$, corresponding to an apparent energy efficiency of 140%. This pragmatic concept promotes energy utilization, vaporization efficiency and water production.

3.6. Photothermal membrane distillation

Membrane distillation (MD) is a hybrid thermal/membrane technology based on the use of microporous hydrophobic membranes, which can distill water at lower temperatures than conventional distillation (i.e., boiling), lower pressures than RO, and maintain the highest salt rejection. Since the hydrorepellent nature of the membrane, liquid filtration is prevented, while mass transfer in vapor phase can take place [100,101]. However, the vapor flux across the membrane and efficiency of conventional MD systems are adversely affected by "temperature polarization", a phenomenon intrinsically related to the removal of latent heat associated with water evaporation [67,102–104]. Solar MD, which is based on direct, localized solar heating of photothermal membrane, can notably increase the feed temperature at the membrane surface, so as to eliminate temperature polarization, thus achieving excellent performance [67,103,105]. Moreover, the localized heating process excludes the prerequisite of the input water heating, eliminating the inherent efficiency limitations and substantial power requirements of the conventional MD process. Halas's group demonstrated a broadband light-absorbing nanoparticles (NPs, carbon black) enabled solar membrane distillation (NESMD) [67]. The localized solar heating of the hybrid membrane led to the vaporization of the feed water, which subsequently transported through the membrane and condensed on the distillate side (Fig. 5e-f). It is experimentally verified that a flux of over $5.38 \text{ kg m}^{-2} \text{ h}^{-1}$ with a solar efficiency of over 20% and greater than 99.5% salt rejection under concentrated solar illumination was delivered. This reveals the NESMD could possibly function as a promising off-grid desalination technology. Furthermore, the performance of NESMD system can be improved by implementing heat recovery scheme via recirculating of the feed output back into the feed input, which would increase the permeated water flux and overall energy efficiency. Since water has a huge evaporation latent heat, the strategy of latent heat recycling instead of giving-off naturally is increasingly important for highly efficient water distillation and maintenance of the temperature difference across the membrane. Zhou's group reported a two-level solar MD device for harvesting water with high solar efficiency and salt rejection, as shown in Fig. 5g [102]. In the water-harvesting process, the vapor induced by solar irradiation was forced to flow downward and condense by cold bulk water. The high temperature difference between the vapor and the collector ensures large driving force to induce the flow while the porous hydrophobic membrane warrants high salt rejection. The two-level collectors were designed for recycling the latent heat. The collectors worked as a condenser, the latent heat released from the first level collector as a thermal source to heat up the next level cold bulk water to generate vapor, further enhancing the water productivity (Fig. 5h). The water productivity was $1.02 \text{ kg m}^{-2} \text{ h}^{-1}$ after the two-level collection, corresponding to a solar efficiency of 72% under solar illumination of 1 kW m^{-2} . Under an outdoor experiment, this device could collect 3.67 kg m^{-2} water per day.

4. Scalable applications of interfacial water evaporation

Emerging large-scale applications of interfacial water evaporation are predominantly demonstrated for clean water production including saline water desalination and wastewater purification, as well as

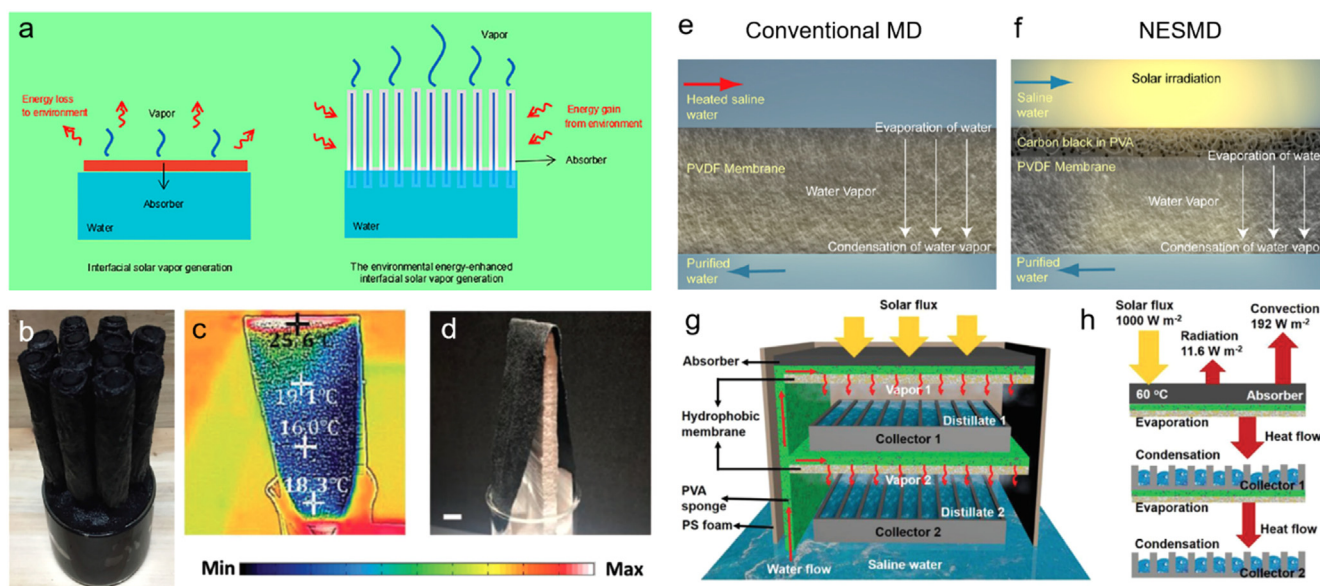


Fig. 5. (a) Schematics of the traditional interfacial solar vapor generator and the environmental energy-enhanced interfacial solar vapor generator. (b) Photograph of the environmental energy-enhanced interfacial solar vapor generator [13]. Reprinted with permission from Ref. [13]. (c) The thermal distribution image and (d) corresponding photograph of CP-foam structures with $\theta = 22.4^\circ$ under 1 sun illumination [98]. Reproduced from Ref. [96]. (CC BY-NC 4.0). Comparison of (e) conventional MD and (f) NESMD [67]. Reprinted from Ref. [66]. (CC BY-NC 4.0). (g) The cross-sectional view of every component of the two-level solar MD system and the water transfer process. (h) Energy balance and heat transfer diagram for an absorber under the solar flux in two-level solar MD [102]. Reprinted with permission from Ref. [100].

electrical energy generation based on tailored optical and thermal features that are beneficial for the solar evaporation process. From the practical viewpoint, we will highlight the recent developments that exemplify the potential of scalable applications in the following section.

4.1. Saline water desalination

Desalination is a process that extracts mineral components from saline water, which is one of the most important and cost-effective approaches to increase the fresh water supply. In direct solar desalination process, the heat source for evaporation is provided by solar energy. However, the low efficiency due to poor solar absorption and massive heat loss limits its practical applications. Efficiency improvements commonly through large optical concentrators are also not feasible for economical large-scale applications. Recently, advancement in solar absorber materials and system designs for interfacial solar-driven evaporation have greatly improved the solar-to-steam conversion efficiency, opening up a possibility of scale-up desalination in a low-cost manner under practical 1 sun illumination [25,106]. Various efficient outdoor solar stills have been developed and employed as large-scale saline water desalination, such as conventional (single basin covered by a single inclined cover) [53,66,69,107–110], conical [79], quasi-spherical [25,111], model house [2,19,24,112] and pyramid prototypes [19,107]. The corresponding relatively large solar absorbers are either directly synthesized [2,26,53,85] or rationally assembled via smaller modules [13,66,87,108], and placed at the bottom of the solar stills. Efficient light absorption, water transport, as well as fresh water condensation and collection within these prototypes have been realized. After the solar desalination, the salinities of the brine water were significantly decreased, surpassing the drinking water standards defined by the World Health Organization (1‰) and the US Environmental Protection Agency (0.5‰). The scalable solar still can obtain adequate potable fresh water for individual daily drinking needs [2,25,110]. Chen's group demonstrated a salt-rejecting evaporation structure that can operate continuously under sunlight to generate clean vapor while floating on a saline body of water [2]. The top layer of black cellulose fabric for the light receiving and localized heating was isolated by an

insulating structure made from alternating layers of EPS foam and white cellulose fabric (Fig. 6a and b). The insulating structure serves to simultaneously thermal insulate the evaporation layer and reject excess salts. With the model house solar still, water collection tests were conducted in a controlled rooftop setup and in the ocean, as shown in Fig. 6c and d. The maximum daily freshwater production rates measured were 2.81 and 2.5 L m⁻² day⁻¹ for the rooftop and ocean testing respectively, which can satisfy individual drinking needs. The entire system's material cost is \$3 m⁻², much lower than conventional solar stills. It does not require energy infrastructure, and can provide the off-grid communities with a good access to affordable clean water. Another prototype of conventional desalination solar still equipped with 5 × 5 CP-foam unit array as solar absorber was reported by Gan's group [66]. The seawater desalination tests were performed both in the laboratory and outdoor environment, the portable solar still showed a water generation rate of 2.4 times higher than that of the commercial product (Aquamate Solar Still) yet at a much lower cost. Yu's group reported a desiccator-like desalination prototype based on a floating hierarchical nanostructured gel [25]. The outdoor experiment was carried out for 12 h under natural sunlight with an average solar heat flux of $\sim 0.7 \text{ kW m}^{-2}$, establishing an average water purification rate of $\sim 1.6 \text{ L m}^{-2} \text{ h}^{-1}$. The water quality was directly monitored by the resistance value which validates the purified water was comparable to the domestic water. This indicates effective purification of natural seawater. The daily yield of fresh water was further estimated to be 18–23 L m⁻² by the prototype under natural sunlight, suggesting its potential for scalable manufacturing and practical applications.

4.2. Wastewater purification

Another important application of interfacial water evaporation is the wastewater purification of domestic and industrial sewage. Like the saline water desalination, similar solar stills are adopted for wastewater purification including sterilization [16,92], degradation of dye molecules [68,92,113], removal of heavy metal ion [45,89] and separation of emulsified oil/water mixtures [92]. Zhu's group illustrated a scalable interfacial solar vapor generator composed of cylindrical arrays of

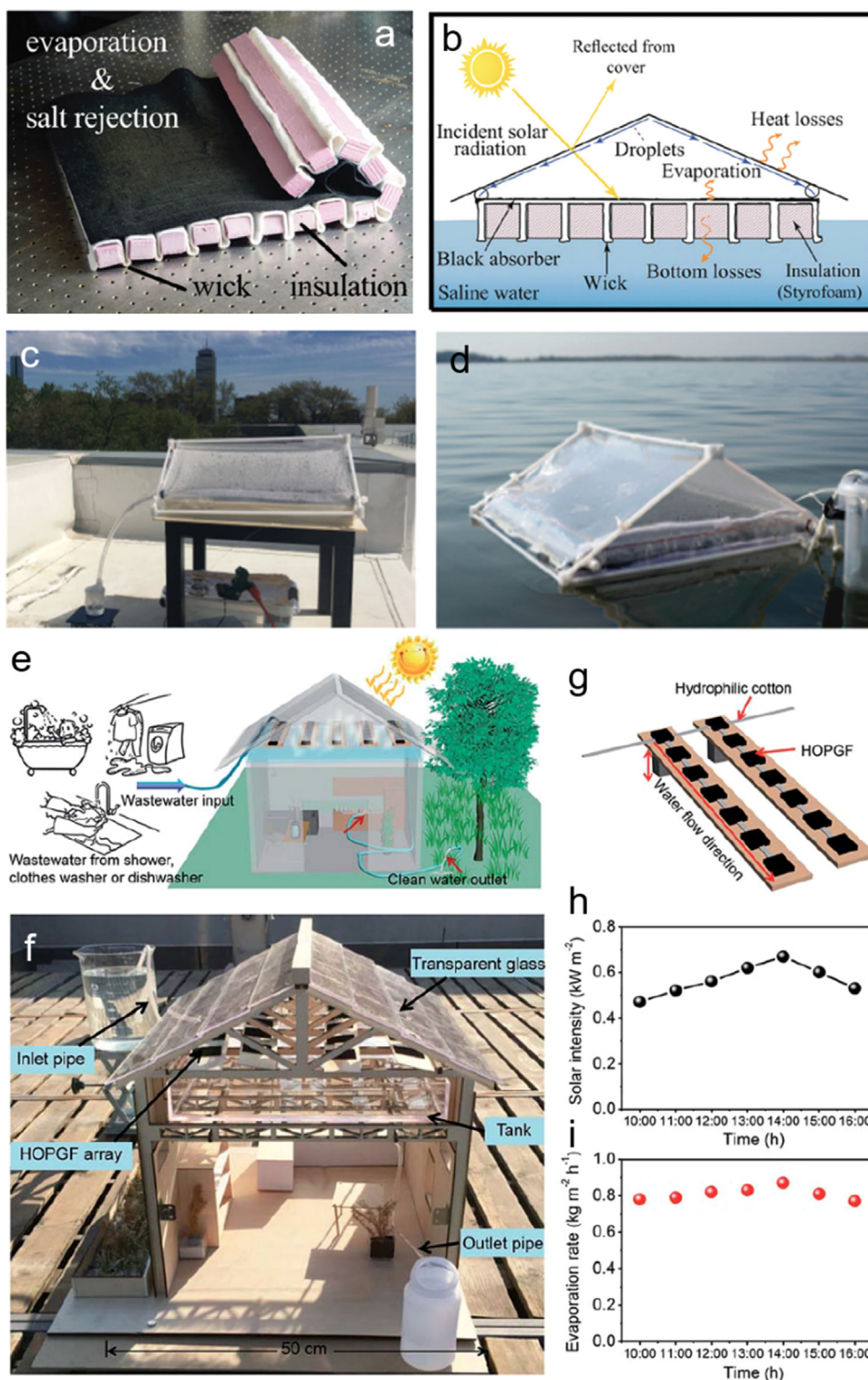


Fig. 6. (a) Photograph of the evaporation structure. (b) Schematic of the evaporation structure in a fabricated polymer-film based condensation cover. Photographs of the solar still in operation on the rooftop (c) and the ocean (d) [2]. Reprinted with permission from Ref. [2]. (e) Schematic illustration of a house supplying clean water based on solar steam generation. (f) Photograph of a lab made house model with a size of 50 cm × 60 cm × 60 cm under the sunlight at Beijing. (g) Schematic illustration of the HOPGF array in the designed house. (h) Outdoor solar intensity and (i) water evaporation rates of the HOPGF system in (f) [87]. Reprinted with permission from Ref. [85].

cotton cores wrapped with carbon black-coated cellulose paper for the heavy metal solution and dye solution treatments [13]. The evaporation rates for the two wastewater solution samples were beyond the theoretical limit under 1 sun due to the lower surface temperature that can gain energy from the environment, as discussed earlier. Under the outdoor environmental conditions, the masses of the heavy metal solution and dye solution were linearly decreased. The concentrations of the Cu^{2+} heavy metal ions in the vapor was 0.066 mg L^{-1} whereas insignificant concentration of Cr^{3+} , and Pb^{2+} were detected ($< 0.01 \text{ mg L}^{-1}$), which were lower than the required concentrations

for effluent discharge in China. The concentration of rhodamine B dye molecules in vapor also decreased from $10^{-5} \text{ mol L}^{-1}$ to below the limit of detection ($10^{-11} \text{ mol L}^{-1}$), indicating the versatility of the wastewater purification. Another approach is by incorporating photocatalysts in the solar absorber material to remove organic dye contaminants through photocatalytic degradation. Besides that, interfacial solar steam off-grid sterilization system was also demonstrated by Zhu's group [16]. A proof-of-concept sterilization prototype with a 10.5 L solar autoclave was built with very low cost and an effective sterilization ($\approx 99.999999\%$ inactivation of pathogen) was achieved, making

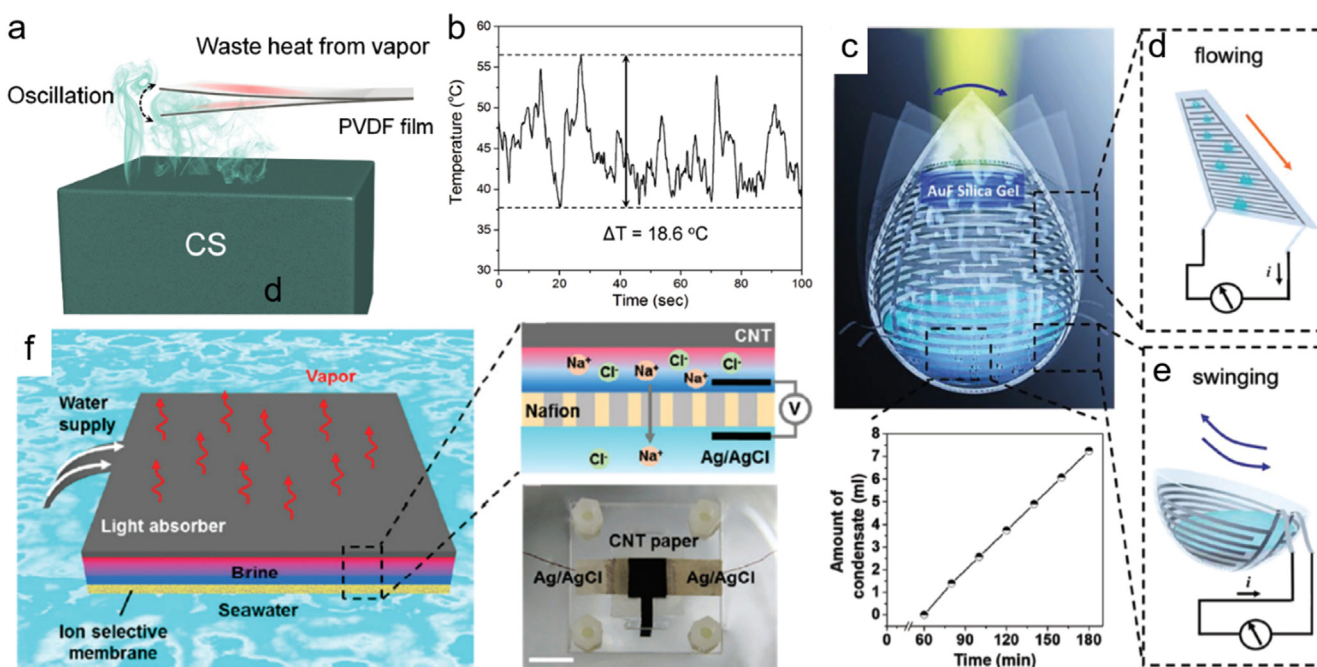


Fig. 7. (a) Schematic diagram of steam generation-induced electric potential by carbon sponge and (b) the temperature fluctuations of the PVDF film surface [19]. Reprinted with permission from Ref. [19]. (c) Schematic diagram of the integral prototype for condensate collection and triboelectric energy generation. Schematic diagram of TENG for (d) water flowing down the wall and (e) water swinging in the round bottom vessel [17]. Reprinted with permission from Ref. [17]. (f) Schematic of the hybrid system for solar desalination and salinity power extraction [120]. Reprinted with permission from Ref. [118].

the solar steam sterilization strategy a promising and complementary personalized solution. Compared with commercialized autoclaves, it showed the higher steam temperature, faster response and better energy-efficiency. Hao et al. demonstrated a bifunctional TiO_2 /polydopamine (PDA)/PPy/cotton to purify dye wastewater through solar vapor generation and photo-degradation [96]. The PDA modified PPy enhanced the surface area of photothermal material for efficient solar generation. It also promoted the separation of photo-generated electron–hole pairs and thus reduced the charge recombination for a high photocatalytic activity of TiO_2 . This bifunctional fabric evaporator can simultaneously achieve a high interfacial solar evaporation rate ($1.55 \text{ kg m}^{-2} \text{ h}^{-1}$) and an effective localized photo-degradation ($\sim 96\%$ degradation of methyl orange for 3 h) under 1 sun illumination. A proof-of-concept housing self-supply water system has been designed by Qu's group using HOPGF as an efficient solar water purification material to realize cyclic utilization of household sewage, such as wastewater from the shower, clothes washer and dishwasher (Fig. 6e) [87]. A house model with the size of $50 \text{ cm} \times 60 \text{ cm} \times 60 \text{ cm}$ was built to verify the feasibility of the system (Fig. 6f). In this system, HOPGF arrays were fixed on the board and then placed on the housetop with one end higher. Hydrophilic cotton was used to connect the HOPGF samples to draw wastewater by the capillary force (Fig. g). The released vapor was condensed on the transparent glass roof and then clean water was collected in the tank for further use. Under natural conditions of the late-autumn sunny day of Beijing (~ 0.6 sun), an average water generation rate of ca. $0.8 \text{ kg m}^{-2} \text{ h}^{-1}$ was achieved (Fig. 6h and i), suggesting the as-designed system may realize cyclic utilization of domestic sewage as an alternative water source.

4.3. Energy generation

Solar-induced energy generation through photovoltaic, photoelectrical and photochemical processes has been widely investigated and shown excellent performance [114–117]. Therefore, it is rational to solve water and energy scarcity issues at the same time by combining the solar vaporization with energy generation. Recently, efficient solar

evaporation process, integrated with tribo- [17], pyro-, piezo- [19] thermo-electric [118,119] or salinity-induced [120] device, has shown to be capable of freshwater production and electricity generation utilizing free sunlight. With the dual functions or concurrent demonstrations of freshwater production and electricity generation, the overall efficiency of photothermal conversion can be ameliorated. Ho's group reported scavenging of the dynamic mechanical and temperature fluctuations for waste heat energy-to-electricity conversion through a ferroelectric fluoropolymer polyvinylidene fluoride (PVDF) which could harvest the otherwise wasted thermomechanical reaction during the solar-vaporization process, as shown in Fig. 7a [19]. Due to the temperature fluctuation derived from the as-generated steam heating–cooling variation on the PVDF film surface (Fig. 7b), the closed-circuit current and open-circuit voltage were measured to be -80 nA and -20 V , respectively. Another hybrid system using the condensation process for electricity generation was also demonstrated by Ho's group [17]. The prototype was fabricated for simultaneous condensate collection and energy generation, as shown in Fig. 7c. The solar induced vapor condensed on the wall of the triboelectric nanogenerator (TENG) where polytetrafluoroethylene (PTFE) film adhered. When the condensate flowed down, the triboelectric signal was generated due to the electrification of the water on the PTFE wall (Fig. 7d). More interestingly, the round-bottom prototype can harvest omnidirectional mechanical energy e.g. wind to swing in random directions Fig. 7e. This induces the movement of the collected condensate on the PTFE lined round bottom vessel, additionally resulting in the triboelectricity generation.

Aside, rapid evaporation of water at the light absorber surface would induce a high salt concentration compared with brine underlying the interface. Take advantage of such salinity gradient, electrical power can be produced. Zhou's group presented a new concept of hybrid energy generation technology using a piece of CNT modified super-hydrophilic filter paper as the light absorber and a commercial Nafion membrane as the ion selective membrane (Fig. 7f) [120]. Solar desalination and electricity extraction from the evaporation induced salinity gradient were realized simultaneously. A high thermal efficiency up to

75% was achieved under 1 sun illumination and an electrical output power of $\sim 1 \text{ W m}^{-2}$ was generated. A proof-of-concept prototype was also constructed to verify the ability of the device to work under natural sunlight and the possibility of scaling-up. Collectively, these works provide an innovative approach for blue energy utilization, demonstrating the potential for simultaneous fresh water and clean electricity generation under natural sunlight on-site or on-demand.

5. Conclusion and perspectives

In recent years, an increasing interest in the development of solar evaporation for clean water production has been witnessed. We have highlighted various solar absorber material and system design concepts that are widely used to enhance interfacial photothermal vaporization. For each concept, we illustrated how it has promoted solar absorptance and/or minimized heat losses, which eventually lead to successful photothermal vaporization. With the innovative photothermal system designs, the interfacial solar steam generation performance has been effectively enhanced, paving a potential way for highly efficient solar steam generation without the use of expensive optical concentrators. Hence, a handful of scalable and practical applications in seawater desalination, wastewater purification and energy generation have been materialized and presented.

However, there are several important challenges that need to be confronted. Still the gap between the current state-of-art and practical applications is considerable. Although the extremely high conversion efficiencies ($> 90\%$, even beyond the theoretical limit) are achieved in lab conditions recently, the outdoor efficiency with the natural solar flux still needs progression, in order for the photothermal technology to be a competitive alternative to the traditional solar steam generation technologies. Moreover, factors including thermal stability, robustness, degradation of materials and systems, reproducibility, ease of transport and storage need further systematic studies before commercializing. Moreover, in solar distillation devices, efficient water condensation and collection strategies, as well as the effective recovery of the latent heat of water condensation are crucial for clean water production, which can significantly boost the energy efficiency. Meanwhile, photothermal mechanisms of various processes, e.g. solar-heat conversion, water transport and heat transfer, demands indepth studies to better evaluate and access the material/system performance. Finally, adding or exploring other correlated functions beyond steam generation represents a promising direction in which one could expand the photothermal opportunities. Rational and efficient designs for integrated applications (sterilization, purification, catalysis, electricity and chemical fuel generation) that interlinked water, energy and environmental nexus in a mutually beneficial ways are needed to bring about sustainable solutions of these inextricably intertwined resources.

Acknowledgements

This work is supported by the Ministry of Education (MOE) under R-263-000-D18-112 grant and Singapore Ministry of National Development and the National Research Foundation, Prime Minister's Office under the Land and Liveability National Innovation Challenge (L2 NIC) Research Programme (L2 NIC Award No. L2NICCF2-2015-3).

References

- [1] P.J.J. Alvarez, C.K. Chan, M. Elimelech, N.J. Halas, D. Villagrán, *Nat. Nanotechnol.* 13 (2018) 634–641.
- [2] G. Ni, S.H. Zandavi, S.M. Javid, S.V. Boriskina, T.A. Cooper, G. Chen, *Energy Environ. Sci.* 11 (2018) 1510–1519.
- [3] L. Zhu, C. Fu Tan, M. Gao, G.W. Ho, *Adv. Mater.* 27 (2015) 7713–7719.
- [4] R. Verbeke, V. Gómez, I.F.J. Vankelecom, *Prog. Polym. Sci.* 72 (2017) 1–15.
- [5] M. Elimelech, W.A. Phillip, *Science* 333 (2011) 712–717.
- [6] A.D. Khawaji, I.K. Kutubkhanah, J.-M. Wie, *Desalination* 221 (2008) 47–69.
- [7] L. Zhu, M. Gao, C.K.N. Peh, G.W. Ho, *Mater. Horiz.* 5 (2018) 323–343.
- [8] L. Zhang, B. Tang, J. Wu, R. Li, P. Wang, *Adv. Mater.* 27 (2015) 4889–4894.
- [9] Y. Liu, S. Yu, R. Feng, A. Bernard, Y. Liu, Y. Zhang, H. Duan, W. Shang, P. Tao, C. Song, T. Deng, *Adv. Mater.* 27 (2015) 2768–2774.
- [10] J. Zhou, Z. Sun, M. Chen, J. Wang, W. Qiao, D. Long, L. Ling, *Adv. Funct. Mater.* 26 (2016) 5368–5375.
- [11] J. Yang, Y. Pang, W. Huang, S.K. Shaw, J. Schiffbauer, M.A. Pillers, X. Mu, S. Luo, T. Zhang, Y. Huang, G. Li, S. Ptasinska, M. Lieberman, T. Luo, *ACS Nano* 11 (2017) 5510–5518.
- [12] Z. Deng, J. Zhou, L. Miao, C. Liu, Y. Peng, L. Sun, S. Tanemura, *J. Mater. Chem. A* 5 (2017) 7691–7709.
- [13] X. Li, J. Li, J. Lu, N. Xu, C. Chen, X. Min, B. Zhu, H. Li, L. Zhou, S. Zhu, T. Zhang, *J. Zhu, Joule* 2 (2018) 1331–1338.
- [14] W. Shang, T. Deng, *Nat. Energy* 1 (2016) 16133.
- [15] V.-D. Dao, H.-S. Choi, *Global Challenges* 2 (2018) 1700094.
- [16] J. Li, M. Du, G. Lv, L. Zhou, X. Li, L. Bertoluzzi, C. Liu, S. Zhu, J. Zhu, *Adv. Mater.* 30 (2018) 1805159.
- [17] M. Gao, C.K. Peh, H.T. Phan, L. Zhu, G.W. Ho, *Adv. Energy Mater.* 8 (2018) 1800711.
- [18] M. Gao, L. Zhu, C.K. Peh, G.W. Ho, *Energy Environ. Sci.* (2019), <https://doi.org/10.1039/C8EE01146J>.
- [19] L. Zhu, M. Gao, C.K.N. Peh, X. Wang, G.W. Ho, *Adv. Energy Mater.* 8 (2018) 1702149.
- [20] G. Liu, J. Xu, K. Wang, *Nano Energy* 41 (2017) 269–284.
- [21] H. Ghasemi, G. Ni, A.M. Marconnet, J. Loomis, S. Yerci, N. Miljkovic, G. Chen, *Nat. Commun.* 5 (2014) 4449.
- [22] X. Hu, W. Xu, L. Zhou, Y. Tan, Y. Wang, S. Zhu, J. Zhu, *Adv. Mater.* 29 (2017) 1604031.
- [23] G. Ni, G. Li, S.V. Boriskina, H. Li, W. Yang, T. Zhang, G. Chen, *Nat. Energy* 1 (2016) 16126.
- [24] L. Zhou, Y. Tan, J. Wang, W. Xu, Y. Yuan, W. Cai, S. Zhu, J. Zhu, *Nat. Photon.* 10 (2016) 393–398.
- [25] F. Zhao, X. Zhou, Y. Shi, X. Qian, M. Alexander, X. Zhao, S. Mendez, R. Yang, L. Qu, G. Yu, *Nat. Nanotechnol.* 13 (2018) 489–495.
- [26] P. Zhang, J. Li, L. Lv, Y. Zhao, L. Qu, *ACS Nano* 11 (2017) 5087–5093.
- [27] J. Wang, Y. Li, L. Deng, N. Wei, Y. Weng, S. Dong, D. Qi, J. Qiu, X. Chen, T. Wu, *Adv. Mater.* 29 (2017) 1603730.
- [28] H. Ren, M. Tang, B. Guan, K. Wang, J. Yang, F. Wang, M. Wang, J. Shan, Z. Chen, D. Wei, H. Peng, Z. Liu, *Adv. Mater.* 29 (2017) 1702590.
- [29] Z.W. Seh, S. Liu, M. Low, S.-Y. Zhang, Z. Liu, A. Mlayah, M.-Y. Han, *Adv. Mater.* 24 (2012) 2310–2314.
- [30] M. Gao, P.K.N. Connor, G.W. Ho, *Energy Environ. Sci.* 9 (2016) 3151–3160.
- [31] R. Long, Y. Li, L. Song, Y. Xiong, *Small* 11 (2015) 3873–3889.
- [32] M.L. Brongersma, N.J. Halas, P. Nordlander, *Nat. Nanotechnol.* 10 (2015) 25.
- [33] S. Linic, U. Aslam, C. Boerigter, M. Morabito, *Nat. Mater.* 14 (2015) 567.
- [34] J.A. Webb, R. Bardhan, *Nanoscale* 6 (2014) 2502–2530.
- [35] K. Jiang, D.A. Smith, A. Pinchuk, *J. Phys. Chem. C* 117 (2013) 27073–27080.
- [36] L. Zhou, Y. Tan, D. Ji, B. Zhu, P. Zhang, J. Xu, Q. Gan, Z. Yu, J. Zhu, *Sci. Adv.* 2 (2016) e1501227.
- [37] M. Zhu, Y. Li, F. Chen, X. Zhu, J. Dai, Y. Li, Z. Yang, X. Yan, J. Song, Y. Wang, E. Hitz, W. Luo, M. Lu, B. Yang, L. Hu, *Adv. Energy Mater.* (2018) 1701028.
- [38] A. Lalisse, G. Tessier, J. Plain, G. Baffou, *J. Phys. Chem. C* 119 (2015) 25518–25528.
- [39] P. Fan, H. Wu, M. Zhong, H. Zhang, B. Bai, G. Jin, *Nanoscale* 8 (2016) 14617–14624.
- [40] A.D. Rakić, A.B. Djurišić, J.M. Elazar, M.L. Majewski, *Appl. Opt.* 37 (1998) 5271–5283.
- [41] C.M. Hessel, V.P. Pattani, M. Rasch, M.G. Panthani, B. Koo, J.W. Tunnell, B.A. Korgel, *Nano Lett.* 11 (2011) 2560–2566.
- [42] X. Huang, W. Zhang, G. Guan, G. Song, R. Zou, J. Hu, *Acc. Chem. Res.* 50 (2017) 2529–2538.
- [43] C. Song, T. Li, W. Guo, Y. Gao, C. Yang, Q. Zhang, D. An, W. Huang, M. Yan, C. Guo, *New J. Chem.* 42 (2018) 3175–3179.
- [44] Z. Hua, B. Li, L. Li, X. Yin, K. Chen, W. Wang, *J. Phys. Chem. C* 121 (2017) 60–69.
- [45] Y. Yang, H. Zhao, Z. Yin, J. Zhao, X. Yin, N. Li, D. Yin, Y. Li, B. Lei, Y. Du, W. Que, *Mater. Horiz.* 5 (2018) 1143–1150.
- [46] G. Zhu, J. Xu, W. Zhao, F. Huang, *ACS Appl. Mater. Interfaces* 8 (2016) 31716–31721.
- [47] M. Ye, J. Jia, Z. Wu, C. Qian, R. Chen, P.G. O'Brien, W. Sun, Y. Dong, G.A. Ozin, *Adv. Energy Mater.* 7 (2017) 1601811.
- [48] Y. Zeng, J. Yao, B.A. Horri, K. Wang, Y. Wu, D. Li, H. Wang, *Energy Environ. Sci.* 4 (2011) 4074–4078.
- [49] R. Chen, Z. Wu, T. Zhang, T. Yu, M. Ye, *RSC Adv.* 7 (2017) 19849–19855.
- [50] X. Wang, G. Ou, N. Wang, H. Wu, *ACS Appl. Mater. Interfaces* 8 (2016) 9194–9199.
- [51] J.D. Yao, Z.Q. Zheng, G.W. Yang, *Nanoscale* 9 (2017) 16396–16403.
- [52] J. Yao, Z. Zheng, G. Yang, *Nanoscale* 10 (2018) 2876–2886.
- [53] L. Yi, S. Ci, S. Luo, P. Shao, Y. Hou, Z. Wen, *Nano Energy* 41 (2017) 600–608.
- [54] H. Liu, X. Zhang, Z. Hong, Z. Pu, Q. Yao, J. Shi, G. Yang, B. Mi, B. Yang, X. Liu, H. Jiang, X. Hu, *Nano Energy* 42 (2017) 115–121.
- [55] D. Ding, W. Huang, C. Song, M. Yan, C. Guo, S. Liu, *Chem. Commun.* 53 (2017) 6744–6747.
- [56] J.R. Vélez-Cordero, J. Hernández-Cordero, *Int. J. Therm. Sci.* 96 (2015) 12–22.
- [57] Y. Wang, L. Zhang, P. Wang, *ACS Sustain. Chem. Eng.* 4 (2016) 1223–1230.
- [58] C. Chen, Y. Li, J. Song, Z. Yang, Y. Kuang, E. Hitz, C. Jia, A. Gong, F. Jiang, J.Y. Zhu, B. Yang, J. Xie, L. Hu, *Adv. Mater.* 29 (2017) 1701756.
- [59] Y. Li, T. Gao, Z. Yang, C. Chen, W. Luo, J. Song, E. Hitz, C. Jia, Y. Zhou, B. Liu, B. Yang, L. Hu, *Adv. Mater.* 29 (2017) 1700981.

- [60] Y. Ito, Y. Tanabe, J. Han, T. Fujita, K. Tanigaki, M. Chen, *Adv. Mater.* 27 (2015) 4302–4307.
- [61] K.-K. Liu, Q. Jiang, S. Tadepalli, R. Raliya, P. Biswas, R.R. Naik, S. Singamaneni, *ACS Appl. Mater. Interfaces* 9 (2017) 7675–7681.
- [62] Q. Jiang, L. Tian, K.K. Liu, S. Tadepalli, R. Raliya, P. Biswas, R.R. Naik, S. Singamaneni, *Adv. Mater.* 28 (2016) 9400–9407.
- [63] Y. Wang, C. Wang, X. Song, S.K. Megarajan, H. Jiang, *J. Mater. Chem. A* 6 (2018) 963–971.
- [64] T. Gao, Y. Li, C. Chen, Z. Yang, Y. Kuang, C. Jia, J. Song, E.M. Hitz, B. Liu, H. Huang, J. Yu, B. Yang, L. Hu, *Small Methods*, 1800176.
- [65] Y. Liu, J. Chen, D. Guo, M. Cao, L. Jiang, *ACS Appl. Mater. Interfaces* 7 (2015) 13645–13652.
- [66] Z. Liu, H. Song, D. Ji, C. Li, A. Cheney, Y. Liu, N. Zhang, X. Zeng, B. Chen, J. Gao, Y. Li, X. Liu, D. Aga, S. Jiang, Z. Yu, Q. Gan, *Global Challenges* 1 (2017) 1600003.
- [67] P.D. Dongare, A. Alabastri, S. Pedersen, K.R. Zodrow, N.J. Hogan, O. Neumann, J. Wu, T. Wang, A. Deshmukh, M. Elimelech, Q. Li, P. Nordlander, N.J. Halas, *Proc. Natl. Acad. Sci.* 114 (2017) 6936–6941.
- [68] M.W. Higgins, A.R. Shakeel Rahman, R.R. Devarapalli, M.V. Shelke, N. Jha, *Sol. Energy* 159 (2018) 800–810.
- [69] X. Lin, J. Chen, Z. Yuan, M. Yang, G. Chen, D. Yu, M. Zhang, W. Hong, X. Chen, *J. Mater. Chem. A* 6 (2018) 4642–4648.
- [70] Q. Chen, Z. Pei, Y. Xu, Z. Li, Y. Yang, Y. Wei, Y. Ji, *Chem. Sci.* 9 (2018) 623–628.
- [71] N. Xu, X. Hu, W. Xu, X. Li, L. Zhou, S. Zhu, *J. Zhu, Adv. Mater.* 29 (2017) 1606762.
- [72] G. Xue, K. Liu, Q. Chen, P. Yang, J. Li, T. Ding, J. Duan, B. Qi, J. Zhou, *ACS Appl. Mater. Interfaces* 9 (2017) 15052–15057.
- [73] C. Jia, Y. Li, Z. Yang, G. Chen, Y. Yao, F. Jiang, Y. Kuang, G. Pastel, H. Xie, B. Yang, S. Das, L. Hu, *Joule* 1 (2017) 588–599.
- [74] H. Chen, L. Shao, T. Ming, Z. Sun, C. Zhao, B. Yang, J. Wang, *Small* 6 (2010) 2272–2280.
- [75] Y. Shi, R. Li, Y. Jin, S. Zhuo, L. Shi, J. Chang, S. Hong, K.-C. Ng, P. Wang, *Joule* 2 (2018) 1171–1186.
- [76] Y. Wang, C. Wang, X. Song, M. Huang, S.K. Megarajan, S.F. Shaikat, H. Jiang, *J. Mater. Chem. A* 6 (2018) 9874–9881.
- [77] K. Kim, S. Yu, C. An, S.-W. Kim, J.-H. Jang, *ACS Appl. Mater. Interfaces* 10 (2018) 15602–15608.
- [78] J. Fang, Q. Liu, W. Zhang, J. Gu, Y. Su, H. Su, C. Guo, D. Zhang, *J. Mater. Chem. A* 5 (2017) 17817–17821.
- [79] Y. Yang, R. Zhao, T. Zhang, K. Zhao, P. Xiao, Y. Ma, P.M. Ajayan, G. Shi, Y. Chen, *ACS Nano* 12 (2018) 829–835.
- [80] G. Wang, Y. Fu, A. Guo, T. Mei, J. Wang, J. Li, X. Wang, *Chem. Mater.* 29 (2017) 5629–5635.
- [81] X. Gao, H. Ren, J. Zhou, R. Du, C. Yin, R. Liu, H. Peng, L. Tong, Z. Liu, J. Zhang, *Chem. Mater.* 29 (2017) 5777–5781.
- [82] P.-F. Liu, L. Miao, Z. Deng, J. Zhou, H. Su, L. Sun, S. Tanemura, W. Cao, F. Jiang, L.-D. Zhao, *Mater. Today Energy* 8 (2018) 166–173.
- [83] S. Yu, Y. Zhang, H. Duan, Y. Liu, X. Quan, P. Tao, W. Shang, J. Wu, C. Song, *T. Deng, Sci. Rep.* 5 (2015) 13600.
- [84] L. Zhou, S. Zhuang, C. He, Y. Tan, Z. Wang, J. Zhu, *Nano Energy* 32 (2017) 195–200.
- [85] T. Li, H. Liu, X. Zhao, G. Chen, J. Dai, G. Pastel, C. Jia, C. Chen, E. Hitz, D. Siddhartha, R. Yang, L. Hu, *Adv. Funct. Mater.* 28 (2018) 1707134.
- [86] H. Liu, C. Chen, G. Chen, Y. Kuang, X. Zhao, J. Song, C. Jia, X. Xu, E. Hitz, H. Xie, S. Wang, F. Jiang, T. Li, Y. Li, A. Gong, R. Yang, S. Das, L. Hu, *Adv. Energy Mater.* 8 (2018) 1701616.
- [87] P. Zhang, Q. Liao, H. Yao, H. Cheng, Y. Huang, C. Yang, L. Jiang, L. Qu, *J. Mater. Chem. A* 6 (2018) 15303–15309.
- [88] Z. Liu, Z. Yang, X. Huang, C. Xuan, J. Xie, H. Fu, Q. Wu, J. Zhang, X. Zhou, Y. Liu, *J. Mater. Chem. A* 5 (2017) 20044–20052.
- [89] Z. Deng, P.-F. Liu, J. Zhou, L. Miao, Y. Peng, H. Su, P. Wang, X. Wang, W. Cao, F. Jiang, L. Sun, S. Tanemura, *Sol. RRL* 2 (2018) 1800073.
- [90] Y. Li, T. Gao, Z. Yang, C. Chen, Y. Kuang, J. Song, C. Jia, E.M. Hitz, B. Yang, L. Hu, *Nano Energy* 41 (2017) 201–209.
- [91] A. Guo, X. Ming, Y. Fu, G. Wang, X. Wang, *ACS Appl. Mater. Interfaces* 9 (2017) 29958–29964.
- [92] P. Zhang, Q. Liao, T. Zhang, H. Cheng, Y. Huang, C. Yang, C. Li, L. Jiang, L. Qu, *Nano Energy* 46 (2018) 415–422.
- [93] X. Li, R. Lin, G. Ni, N. Xu, X. Hu, B. Zhu, G. Lv, J. Li, S. Zhu, J. Zhu, *Natl. Sci. Rev.* 5 (2018) 70–77.
- [94] X. Li, W. Xu, M. Tang, L. Zhou, B. Zhu, S. Zhu, J. Zhu, *Proc. Natl. Acad. Sci.* 113 (2016) 13953–13958.
- [95] L. Shi, Y. Wang, L. Zhang, P. Wang, *J. Mater. Chem. A* 5 (2017) 16212–16219.
- [96] D. Hao, Y. Yang, B. Xu, Z. Cai, *ACS Sustain. Chem. Eng.* 6 (2018) 10789–10797.
- [97] Q. Zhang, X. Xiao, G. Wang, X. Ming, X. Liu, H. Wang, H. Yang, W. Xu, X. Wang, *J. Mater. Chem. A* 6 (2018) 17212–17219.
- [98] H. Song, Y. Liu, Z. Liu, M.H. Singer, C. Li, A.R. Cheney, D. Ji, L. Zhou, N. Zhang, X. Zeng, Z. Bei, Z. Yu, S. Jiang, Q. Gan, *Adv. Sci.* 5 (2018) 1800222.
- [99] X. Zhou, F. Zhao, Y. Guo, Y. Zhang, G. Yu, *Energy Environ. Sci.* 11 (2018) 1985–1992.
- [100] M. Fujiwara, T. Imura, *ACS Nano* 9 (2015) 5705–5712.
- [101] H.C. Duong, L. Xia, Z. Ma, P. Cooper, W. Ela, L.D. Nghiem, *J. Membr. Sci.* 542 (2017) 133–142.
- [102] G. Xue, Q. Chen, S. Lin, J. Duan, P. Yang, K. Liu, J. Li, J. Zhou, *Global Challenges* 2 (2018) 1800001.
- [103] A. Politano, P. Argurio, G. Di Profio, V. Sanna, A. Cupolillo, S. Chakraborty, H.A. Ararat, E. Curcio, *Adv. Mater.* 29 (2017) 1603504.
- [104] J. Wu, K.R. Zodrow, P.B. Szemraj, Q. Li, *J. Mater. Chem. A* 5 (2017) 23712–23719.
- [105] M. Fujiwara, M. Kikuchi, *Water Res.* 127 (2017) 96–103.
- [106] X. Gao, H. Lan, S. Li, X. Lu, M. Zeng, X. Gao, Q. Wang, G. Zhou, J.-M. Liu, M.J. Naughton, K. Kempa, J. Gao, *Glob. Challenges* 2 (2018) 1800035.
- [107] K.H. Nayi, K.V. Modi, *Renew. Sustain. Energy Rev.* 81 (2018) 136–148.
- [108] L. Cui, P. Zhang, Y. Xiao, Y. Liang, H. Liang, Z. Cheng, L. Qu, *Adv. Mater.* 30 (2018) 1706805.
- [109] Z. Wang, Q. Ye, X. Liang, J. Xu, C. Chang, C. Song, W. Shang, J. Wu, P. Tao, T. Deng, *J. Mater. Chem. A* 5 (2017) 16359–16368.
- [110] J. Xu, F. Xu, M. Qian, Z. Li, P. Sun, Z. Hong, F. Huang, *Nano Energy* 53 (2018) 425–431.
- [111] Y. Yang, X. Yang, L. Fu, M. Zou, A. Cao, Y. Du, Q. Yuan, C.-H. Yan, *ACS Energy Lett.* 3 (2018) 1165–1171.
- [112] X. Wu, L. Wu, J. Tan, G.Y. Chen, G. Owens, H. Xu, *J. Mater. Chem. A* 6 (2018) 12267–12274.
- [113] H.D. Kirirachchi, F.S. Awad, A.A. Hassan, J.A. Bobb, A. Lin, M.S. El-Shall, *Nanoscale* 10 (2018) 18531–18539.
- [114] X.-Q. Wang, C.F. Tan, K.H. Chan, X. Lu, L. Zhu, S.-W. Kim, G.W. Ho, *Nat. Commun.* 9 (2018) 3438.
- [115] T. Ding, L. Zhu, X.-Q. Wang, K.H. Chan, X. Lu, Y. Cheng, G.W. Ho, *Adv. Energy Mater.* 8 (2018) 1802397.
- [116] M.-Q. Yang, M. Gao, M. Hong, G.W. Ho, *Adv. Mater.* 30 (2018) 1802894.
- [117] L. Zhu, M. Hong, G.W. Ho, *Nano Energy* 11 (2015) 28–37.
- [118] L. Zong, M. Li, C. Li, *Nano Energy* 50 (2018) 308–315.
- [119] X. Li, X. Min, J. Li, N. Xu, P. Zhu, B. Zhu, S. Zhu, J. Zhu, *Joule* 2 (2018) 2477–2484.
- [120] P. Yang, K. Liu, Q. Chen, J. Li, J. Duan, G. Xue, Z. Xu, W. Xie, J. Zhou, *Energy Environ. Sci.* 10 (2017) 1923–1927.